Type of the Paper (Article, Review, Communication, etc.)

$NiCo_2O_4$-based Hybrid Nanocomposite for High-Performance Pseudocapacitor Electrodes

Mehdi Eskandari [1,2], Rasoul Malekfar [1], David Buceta [3] and Pablo Taboada [2,*]

[1] Atomic and Molecular Group, Physics Department, Faculty of Basic Sciences, Tarbiat Modares University, 14115-111 Tehran, I.R. Iran; Mehdi.eskandari.phys@gmail.com
[2] Colloids and Polymer Physics Group, Department of Particle Physics, Faculty of Physics, Campus Vida, Universidade de Santiago de Compostela, 15782 Santiago de Compostela Spain
[3] NANOMAG Laboratory, Departments of Physical Chemistry and Applied Physics, IIT, Campus Vida, Universidade de Santiago de Compostela, 15782 Santiago de Compostela, Spain
* Correspondence: pablo.taboada@usc.es; Tel.: +34-881-814-111 (F.L.)

Received: date; Accepted: date; Published: date

Abstract: New hybrid nanostructured electrodes for supercapacitors made by combination of electrical double layer and faradaic supercapacitors based-nanomaterials within a single hybrid composite has a great potential on expanding the range of use of these devices and increase their electrochemical performance. In this work, we developed several hybrid nanostructured composites with combinations of such types of materials with potential applicability as electrodes in supercapacitors. In particular, these composites were obtained by easy, cost-effective and scalable procedures, and were composed by $NiCo_2O_4$ nanocores as the main faradaic-based nanomaterial and either the conductive polymer polyaniline (PANI), multiwall carbon nanotubes (MWCNTs), or reduced graphene oxide (r-GO) as the electrical double layer-based carbonaceous-based nanomaterials in order to enable the combination of both type of energy storage processes within a single nanostructured device. These constructions allowed us to obtain specific capacitance as large as 1760 F/g, 900 F/g and 734 F/g at a current density of 1 A/g for $NiCo_2O_4$/PANI, $NiCo_2O_4$/MWCNT, and $NiCo_2O_4$/r-GO hybrid nanocomposite electrodes, respectively. Besides, the stability of $NiCo_2O_4$/MWCNTs and $NiCo_2O_4$/r-GO-based electrodes was outstanding, with capacity losses below 10% after long periods of operation (> 500 cycles).

Keywords: $NiCo_2O_4$ nanocores, hybrid nancomposite, carbon-based materials, electrochemical capacitance, supercapacitor

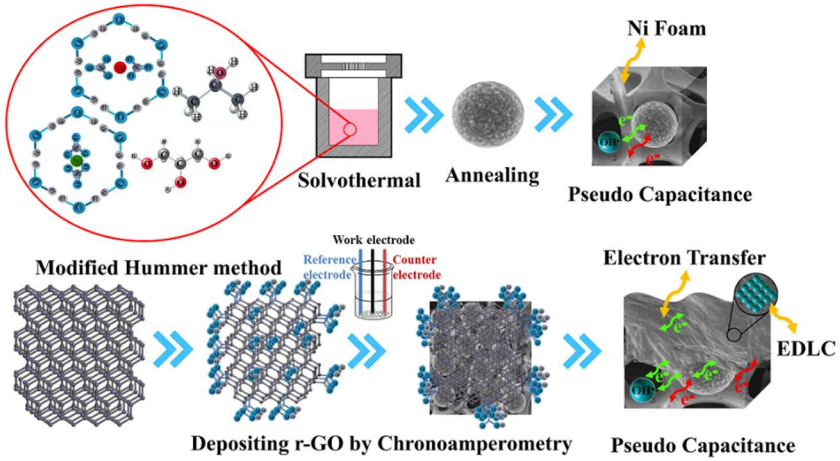

Scheme 1. Graphical abstract

 doi:10.20944/preprints201905.0068.v1

1. Introduction

In the last decades, energy has become one of the most important bottlenecks to further improve human wellbeing. In order to break the excessive energy dependence from fossil fuels, significant progresses on renewable energy technologies such as solar and wind power, hydroelectricity, and biomass have been extensively done [1]. Nevertheless, the dependence of renewable sources and related energy production on environmental conditions together with the increasing use of these "clean" energies effectively require a strong development of energy devices to store and deliver the produced energy on demand. Although different types of storage devices to harvest renewable energy such as fuel cells, lithium-ion batteries, and solar cells to cite a few, are already available even in the market this type of energy devices still need further development to fulfill a plethora of suitable operation conditions as large efficiencies, storage capacities, and charge/discharge powers [2].

Supercapacitors have recently attracted a great deal of interest in various applications including the development of hybrid electric vehicles, large industrial equipment, memory back-up devices and renewable energy power plants thanks to their high power density, fast charge/discharge rates, and long cycle life times [3]. There exist two main classes of supercapacitors, which include electrical double layer (EDLCs) and faradaic supercapacitors (FSs) or pseudocapacitors, respectively. EDLCs bridge the gap between batteries, which offer a high-energy storage capacity (energy density, ED) but a slow charge−discharge, and conventional capacitors that comparatively possess larger power densities (PDs, that is, faster charge−discharge processes) but hold a much lower energy storage capacity. EDLCs typically are made of carbon-based materials bearing high surface area and porosity. They store energy by forming an ionic double layer which diffuses very quickly, hence, providing a very rapid discharge profile as well as high power densities [4]. However, EDs and charges which can be physically stored within EDLCs are still quite low in aqueous as well as organic electrolytes [5]. To overcome these issues, relatively new carbon-based nanomaterials such as one dimensional carbon nanotubes (CNTs) and two-dimensional graphene have been increasingly used to provide higher charge−discharge rates; however, they exhibit a lower volumetric capacitance compared to that of traditional porous carbons [6].

Conversely, FSs use reversible Faradaic reactions to store electrical charges, which allows to achieving higher capacitance and energy densities by at least one order of magnitude than those obtained by EDLCs. Materials sustaining such redox reactions on their surfaces include, for example, conducting polymers and transition metal oxides [7-9]. Conducting polymers have been also used in FSs as a result of their highly π-conjugated polymeric chains, environmental stability and outstanding electrochemical properties [10, 11]. In this regard, polyaniline (PANI) is one of the most significant conductive fillers because of its easy synthesis, low cost, high electrical conductivity and reduced ecotoxicity [12, 13]. On the other hand, ternary metal oxides are another new class of electrode materials for supercapacitors with excellent electrochemical performances, which provide additional free space to enhance the mobility of active species, and reduce the structural strain of electrodes [14]. In particular, metal oxide-based spinel structures are able to provide much larger mobilities of the active species with outstanding electrochemical stability [15]. Amongst spinel ternary metal oxides, nickel cobaltite ($NiCo_2O_4$) has been considered as a very interesting, cost-effective and scalable material thanks to its low cost, abundance, environmental friendliness, and larger electrical conductivity compared to pure nickel and cobalt oxides [16,17]. As a consequence, nickel cobaltite is expected to display much more effective redox reactions than the respective pure oxides thanks to the larger density of active sites and its open structure, which favor an enhanced mobility of charge carriers [15].

Nevertheless, the former two types of materials also display a series of drawbacks as, for example, their poor ion/electron conductivity which limits attainable high capacities at high charge/discharge rates [18, 19] and, in the particular case of metal oxides, the distortion and volume change-induced stress of their microstructure stemming from the continuous supported redox reactions [20], which severely limit the attainable theoretical capacity at high charge/discharge rates. One strategy to improve the electrochemical performance of FSs supercapacitors while avoiding some of the aforementioned drawbacks involves the construction of hybrid nanostructures, which

 doi:10.20944/preprints201905.0068.v1

combine EDLCs and FSs materials in a single nanocomposite. This type of nanostructures not only expands the potential range of use and the effective performance of an active FS nanomaterial as a metal oxide, but also improves the electronic conductivity and charge/discharge rates of the resulting hybrid nanomaterials by using conductive EDLCs carbonaceous materials such as porous carbon, CNTs, graphene, graphene oxide (GO) sheets, etc [21-23]. Moreover, these hybrid nanocomposites possess the capability of preserving the structural integrity of the active metal oxide material, thereby, allowing an enhanced cyclability and rate capacity [24].

Hence, we here report the fabrication of different nanocomposites composed of $NiCo_2O_4$ nanocores as the main FS nanomaterial and carbon allotropes. The combination of $NiCo_2O_4$ nanoparticles (NPs) with carbon-based nanomaterials gives the opportunity to exploit the excellent electrical conductivity and large activated surface areas of the latter as well as the ultrahigh specific capacitance of the former [25]; that is, carbon materials with large contact areas make possible to transfer fast electrons and allow a deeper penetration of electrolyte ions into the hybrid storage nanocomposite. Therefore, the resulting hybrid nanostructured materials including $NiCo_2O_4$ and a carbon allotrope can improve the capacitance of energy storage supercapacitors by sharing the advantages of both classes of materials, which have a synergistic positive effect in the device operation and performance [26]. In addition, the nanostructuration of $NiCo_2O_4$ in the form of NPs should allow a better accommodation of induced mechanical stresses [27, 28], shorten the electron transport lengths, and provide a larger electrode surface. Therefore, $NiCo_2O_4$ nanocores obtained through a solvothermal method [2, 25] were combined with either PANI or multi-wall CNTs (MWCNTs) since these fillers improve the electrical conductivity and activated surface areas of the resulting composite nanostructured materials. In the case of $NiCo_2O_4$/MWCNTs composite, a simple solution mixing methodology was followed to obtain the nanocomposite, which facilitates large scale production while ensuring outstanding electrochemical performances at much lower electrolyte concentrations than commonly used [29,30]. In an alternative configuration, $NiCo_2O_4$ NCs were also deposited on top of a nickel foam substrate and combined with reduced-graphene oxide (r-GO) to improve the electrochemical properties of the metal oxide while avoiding the use of other carbon active materials or isolating binders as polyvinylidene fluoride (PVDF). This procedure for $NiCo_2O_4$/r-GO production is easy, binder free, affordable and more efficient than previously developed, allowing the obtaining of very high capacitances (up to ca. 1760 F/g at 1A/g) thanks to the improvement of the contact between r-GO nanosheets with the metal oxide [31-34]. X-ray diffraction (XRD), Raman spectroscopy, field emission scanning electron microscopy (FESEM), transmission electron microscopy (TEM), and Brunauer-Emmett-Teller (BET) techniques were used to structurally characterize the resulting hybrid nancomposites. Furthermore, the electrochemical performances of the prepared $NiCo_2O_4$/PANI, $NiCo_2O_4$/MWCNT, and $NiCo_2O_4$/r-GO derived nanoelectrodes were characterized by cyclic voltammetry (CV), galvanostatic charge/discharge and electrochemical impedance spectroscopies (EIS). To analyze the obtained impedance experimental data, Zview software was used to design the equivalent theoretical circuit. According to the equivalent circuit elements of $NiCo_2O_4$ nanocores, $NiCo_2O_4$/PANI, $NiCo_2O_4$/MWCNT and $NiCo_2O_4$/r-GO composites, the electrochemical behavior of the constructed supercapacitor electrodes was deciphered.

2. Experimental section

2.1 Materials

Co $(NO_3)_2 \cdot 6H_2O$ and Ni $(NO_3)_2 \cdot 6H_2O$ were purchased from Sigma Aldrich. 2-isopropanol and glycerin were purchased from Merck. Multi-walled carbon nanotubes (MWCNTs, outer diameter 20–30 nm, average length ~50 μm, specific surface area ~110 $m^2\ g^{-1}$ and purity > 95 wt%) were purchased from Neunano, Iran. Aniline, sodium dodecyl sulfate (SDS) and ammonium per sulfate (APS) were also purchased from Sigma Aldrich.

 doi:10.20944/preprints201905.0068.v1

2.2 Synthesis of materials

2.2.1 Synthesis of $NiCo_2O_4$ nanocores

$NiCo_2O_4$ nanocores were prepared based on a previously reported methodology with little modifications [35]. Briefly, 70 mg of cobalt nitrate and 30 mg nickel nitrate were dispersed in 5 mL 2-isopropanol. Then, this solution was added to a mixture of isopropanol (30 mL) and glycerin (8 mL). The resulting solution was poured into a sealed Teflon stainless steel autoclave and put in the oven at 180 °C for 6 h. Then, the solution was washed with ethanol several times and dried at 70 °C. The resulting powder was put in the oven at 350 °C at a heating rate of 1°C/min for 2 h.

2.2.2 Purification of MWCNTs

To purify the MWCNTs, a combined heating an acidic treatment was used [36,37]. Firstly, MWCNTs were heated in an oven at 300°C for 1 h to remove amorphous carbon [38], and then refluxed with HNO_3 for 12 h at 120°C to remove other remaining impurities [39]. The resulting purified MWCNTs were washed several times with DI water to reach neutral pH.

2.2.3 Preparation of $NiCo_2O_4$/MWCNTs, $NiCo_2O_4$/PANI and $NiCo_2O_4$/r-GO nanocomposites

$NiCo_2O_4$/MWCNTs nanocomposites were prepared based on a previously reported method [38]. Briefly, both the starting metal oxide and carbonaceous material were firstly mixed at a weight ratio of 2:1. Then, the mixed powder was dissolved in 2-isopropanol and kept in an ultrasonic bath for 6 h. Next, the dispersed solution was heated at 70 °C to evaporate the solvent.

To prepare $NiCo_2O_4$/PANI nanocomposites, $NiCo_2O_4$ nanocores were dispersed in double-ionised (DI) water (50 mL). Then, SDS (0.08 g) and APS (0.01 g) were dispersed in the former solution, which was held at room temperature for 12 h. Then, aniline (8 µl) was added under stirring at 4 °C. An amount (50 µl) of hydroxide acid (1 M) was added to the previous solution to keep the pH at 3.0. The resulting solution was stirred for 24 h at 4 °C and, then, washed several times with DI water and ethanol [40]. To prepare the $NiCo_2O_4$ nanocores, $NiCo_2O_4$/PANI and $NiCo_2O_4$/MWCNTs electrodes, the obtained active hybrid nanocomposite materials (85 wt. %), carbon black (10 wt. %) and PVDF (5 wt. %) were dispersed in 2 mL acetone. The mixed solution was dropped on a nickel foam substrate, and then dried at 70°C for 7 h to evaporate the solvent.

For the preparation of the $NiCo_2O_4$/r-GO electrodes, $NiCo_2O_4$ nanocores were dispersed in acetone. Then, this solution was slowly dropped onto a nickel foam substrate using a micro-sampler and left in the oven at 70°C for 7 h to evaporate the solvent. Next, graphene oxide was synthesized through a well-established methodology [41], and a solution of GO in DI water (1 mg/mL) prepared. To reduce and deposit GO onto the nickel foam the chronoamperometry method was used at a voltage of -1.6V, as previously reported [42,43].

2.3 Physical characterization

The crystallization of the metal oxide nanocores and the crystalline structure of the nanocomposites were analyzed by means of an X-ray diffractometer (X'pert model 1480 manufactured by Philips) with CuKα radiation. The X-ray wavelength was 1.54056 Å, and the diffraction patterns were recorded at room temperature and over a 2θ range of 10- 80°, at a scanning speed of 2° per minute. Surface area and size distributions of the metal oxide nanocores were measured using a Micromeritics instrument 3020 under nitrogen atmosphere and determined following Brunauer–Emmett–Teller (BET) and Barrett–Joyner–Halenda (BJH) methods. The morphology of the obtained nanocomposites was analyzed by field-emission scanning electron (FESEM) (ZEISS Sigma, manufactured by Germany) and transmission electron microscopies (TEM, Philips CM30).

Finally, the electrochemical properties and performance of the obtained hybrid nanocomposites-based electrodes were determined by cyclic voltammetry (CV), galvanostatic charge/discharge (GCD) curves and electrochemical impedance spectroscopy (EIS) using a SP-300 Bio-Logic potentiostats/galvanostats instrument at room temperature. All tests were performed using a three-electrode setup in which nanocomposite samples, platinum, and Hg/HgO were selected as the

Preprints (www.preprints.org) | NOT PEER-REVIEWED | Posted: 7 May 2019 doi:10.20944/preprints201905.0068.v1

working, counter and reference electrodes, respectively. Electrodes were immersed in 3 M KOH used as the electrolyte. CV tests were repeated for all different types of electrodes at various scan rates ranging from 5 to 50 mVs^{-1} within the potential window of 0.1 to 0.5 V vs. Hg/HgO. GCD measurements were performed by chronopotentiometry (CP) at various current densities. EIS measurements were recorded within the frequency range of 100 kHz–0.1 Hz.

3. Results and Discussion

3.1 Structural characterization

The crystalline phases of $NiCo_2O_4$ nanocores, $NiCo_2O_4$/MWCNT, $NiCo_2O_4$/PANI, and $NiCo_2O_4$/r-GO nanocomposites were investigated by X-ray diffraction. As illustrated in Figure 1a, the diffraction peaks of the spinel phase of $NiCo_2O_4$ nanocores are observed at 2θ values of 22°, 36.3°, 42.8°, 44.9°, 52.3°, 69.8° and 77.1°, which can be indexed to (111), (220), (311), (222), (400), (511), and (440) planes in the face centered cubic spinel structure (JCPDS card No. 20-0781), and matched very well with previously reported data [35,44-47]. $NiCo_2O_4$ as a binary metal oxide has a cubic spinel structure in which all nickel ions occupy octahedral sites, whereas cobalt ions distribute on both octahedral and tetrahedral ones [2,25]. The obtained crystallite size of the nanocores using the Scherrer equation was ca. 256.3 nm.

Regarding $NiCo_2O_4$/PANI nanocomposites, the presence of the conductive polymer does not affect the crystallinity of the metal oxide phase, and the soft slope observed in the XRD pattern (Figure 1) can be assigned to the periodicity of the repeat units of PANI chains parallel to the polymer backbone [48]. A similar diffraction pattern for $NiCo_2O_4$/MWCNTs nanocomposites was also noted, but with additional peaks detected at 30º, 47º and 65º attributed to (002), (100) and (004) reflection planes of the carbonaceous phase, respectively, and related to the hexagonal graphite structures of MWCNTs (JCPDS card No. 41-1487) [47]. Finally, the XRD patterns of $NiCo_2O_4$/r-GO nanocomposites showed some sharp peaks at 45º, 52º, and 76º corresponding to the nickel foam substrate [49]; those corresponding to nickel cobaltite are much smaller but still present [50].

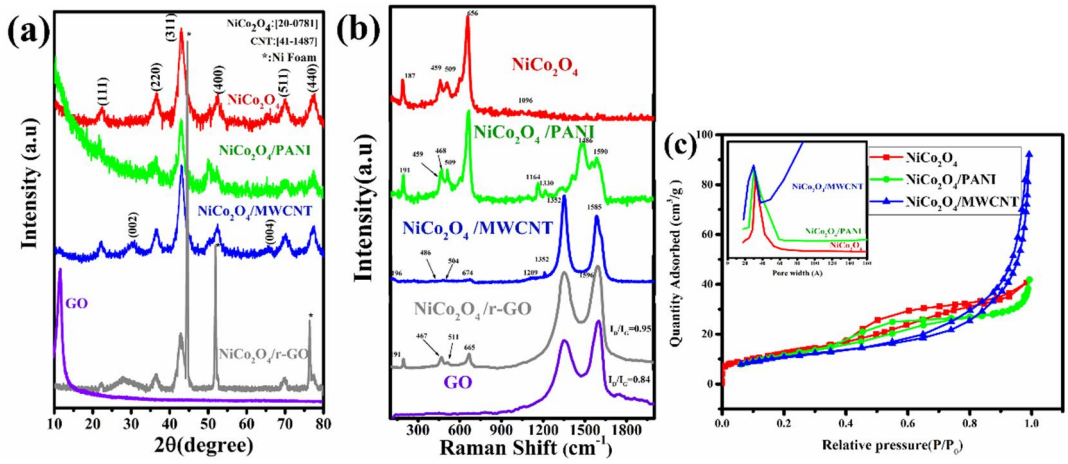

Figure 1: (a) XRD patterns and (b) Raman spectra of $NiCo_2O_4$, $NiCo_2O_4$/PANI, $NiCo_2O_4$/MWCNT and $NiCo_2O_4$/r-GO nanocomposites. (c) N_2 adsorption–desorption isotherms of $NiCo_2O_4$ nanocores, $NiCo_2O_4$/PANI, and $NiCo_2O_4$/MWCNT nanocomposite and their corresponding BJH pore size distributions.

Raman spectroscopy was additionally used to further complete the structural characterization of the obtained hybrid nanocomposites. The 100 to 2000 cm^{-1} regions of the Raman spectra of $NiCo_2O_4$ nanocores, $NiCo_2O_4$/PANI, $NiCo_2O_4$/MWCNTs, $NiCo_2O_4$/r-GO nanocomposites are shown in Figure 1b. Vibrational modes of $NiCo_2O_4$ nanocores are presented at 187, 459, 509, 656, and 1096 cm^{-1}, respectively [44,51], which correspond to F_{2g}, E_g, LO, A_{1g}, and 2 LO modes of the $NiCo_2O_4$ spinel phase [34,52]. Raman spectra of $NiCo_2O_4$/PANI displays the PANI characteristic vibration peaks including the bands attributed to the C–N^+ vibration of delocalized polaronic structures at 1330 cm^{-1}, C=N

 doi:10.20944/preprints201905.0068.v1

stretching at 1486 cm^{-1}, and C–C stretching modes at 1590 cm^{-1}, respectively [53-55]. For $NiCo_2O_4$/MWCNTs nanocomposite, bands at 191, 459, 468, 509 and 665 cm^{-1} attributed to the F_{2g}, E_g, F_{2g}, LO and A_{1g} modes of $NiCo_2O_4$, respectively, are observed while peaks at 1352 and 1585 cm^{-1} correspond to D and G bands of the carbon phase of MWCNTs [46,57]. Moreover, a single G peak at 1585 cm^{-1} proved the multiwall nature of the used CNTs [58]. In Figure 1b also showed peaks at 1352, 1594 cm^{-1} corresponding to D and G, bands of grapheme in $NiCo_2O_4$/r-GO nanocomposites. 2D and D+G bands are attributed to the substantial removal of oxygen-containing groups during the GO reduction process [59]. The reduction of GO nanosheets has a great influence on the electrical conductivity and should allow achieving much larger current discharge capacities [21]. Furthermore, the intensity ratio between D and G bands (I_D/I_G) for GO and $NiCo_2O_4$/r-GO nanocomposites (0.84 and 0.94, respectively) confirms the reduction of GO to r-GO after the chronoamperometric treatment used for the nanocomposite production [60].

BET specific surface areas of $NiCo_2O_4$ nanocores, $NiCo_2O_4$/PANI and $NiCo_2O_4$/MWCNT nanocomposites were determined by N_2 adsorption/desorption isotherms at 77 K, and the corresponding pore size distributions calculated by the Barrette-Joynere-Halenda (BJH) method. For $NiCo_2O_4$/r-GO nanocomposites no adsorption data were obtained due to the different procedure followed for the production of this nanocomposite which impedes this type of measurement, that is, r-GO nanosheets completely covered and support $NiCo_2O_4$ nanocores on the surface of the nickel foam substrates precluding BET analysis. As shown in Figure 1c, the observed adsorption isotherms for both bare $NiCo_2O_4$ nanocores and $NiCo_2O_4$/PANI nanocomposites can be considered as type IV; the hysteresis loop can be related to the formation of a mesoporous material with pore widths with sizes between 2 and 50 nm. Based on the BET analysis, the specific surface area of $NiCo_2O_4$ nanocores and $NiCo_2O_4$/PANI nanocomposites were ca. 39.78 m^2/g and 44.02 m^2/g, respectively. Besides, according to the BJH analysis the center of both distributions was located at ca. 3 and 3.2 nm for $NiCo_2O_4$ nanocores and $NiCo_2O_4$/PANI composites, respectively [30,61,62]. Additionally, the profile and hysteresis loop of $NiCo_2O_4$/MWCNT nanocomposites also denote a type IV isotherm, with a specific surface area of 63.1 m^2/g and pore size distribution of 3 nm and 39.7 nm, respectively, originated from $NiCo_2O_4$ nanocores and MWCNT respectively (see Figure S1)

The surface morphology of the obtained metal oxide nanocores and nanocomposites were additionally investigated by means of FESEM. $NiCo_2O_4$ nanocores appear highly uniform, with relatively smooth surfaces and diameters between 250-300 nm (Figure 2a), in agreement with derived sizes from XRD data. Besides, $NiCo_2O_4$ surfaces become rougher and more porous upon oxidation (see inset in Figure 2a) confirming the high surface area values obtained through nitrogen adsorption experiments. This nanostructuration should enable the formation of suitable channels for an effective ion/electron transfer. Regarding $NiCo_2O_4$/PANI nanocomposites it is clearly observed that $NiCo_2O_4$ nanocores were uniformly covered by PANI (Figure 2b). Conversely, in the case of $NiCo_2O_4$/MWCNTs nanocomposite $NiCo_2O_4$ nanocores seem to be attached to MWCNTs walls and distributed uniformly (Figure 2c). Finally, Figure 2d confirms that r-GO sheets completely cover $NiCo_2O_4$ nanocores onto the surface of the porous nickel foam in $NiCo_2O_4$/r-GO nanocomposites.

 doi:10.20944/preprints201905.0068.v1

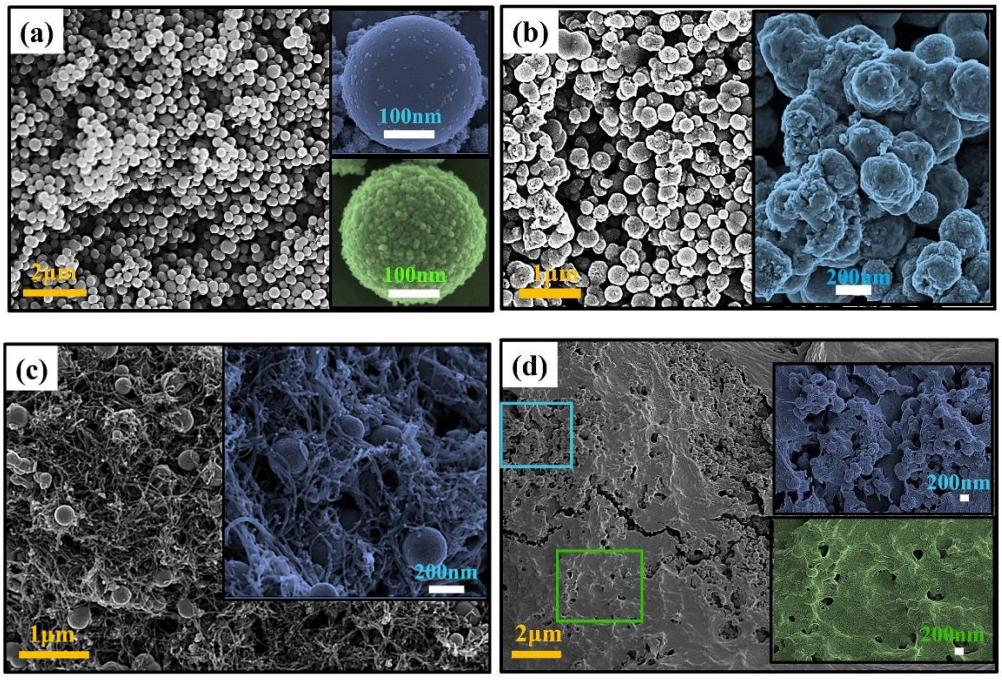

Figure 2: SEM images of (a) $NiCo_2O_4$ nanocores, (b) $NiCo_2O_4$/PANI, (c) $NiCo_2O_4$/MWCNTs, and d,e,f) $NiCo_2O_4$/r-GO nanocomposites. Inset in Figure 2(a): $NiCo_2O_4$ nanocores after the first hour (top) and at the end of the oxidation process (down).

3.2 Electrochemical performance

Cyclic voltammetry was performed to determine the electrochemical capacity and performance of $NiCo_2O_4$ nanocores, $NiCo_2O_4$/PANI, $NiCo_2O_4$/MWCNT and $NiCo_2O_4$/r-GO nanocomposites in a standard three-electrode cell configuration. As observed in Figure 3a, redox peaks are very clear during the cathodic sweeps as a result of faradic redox reactions related to M-O/M-O-OH (M represents Ni or Co) [30,35], which are the origin of the pseudocapacitive characteristics of the nanocomposite [35,63].

Preprints (www.preprints.org) | NOT PEER-REVIEWED | Posted: 7 May 2019 doi:10.20944/preprints201905.0068.v1

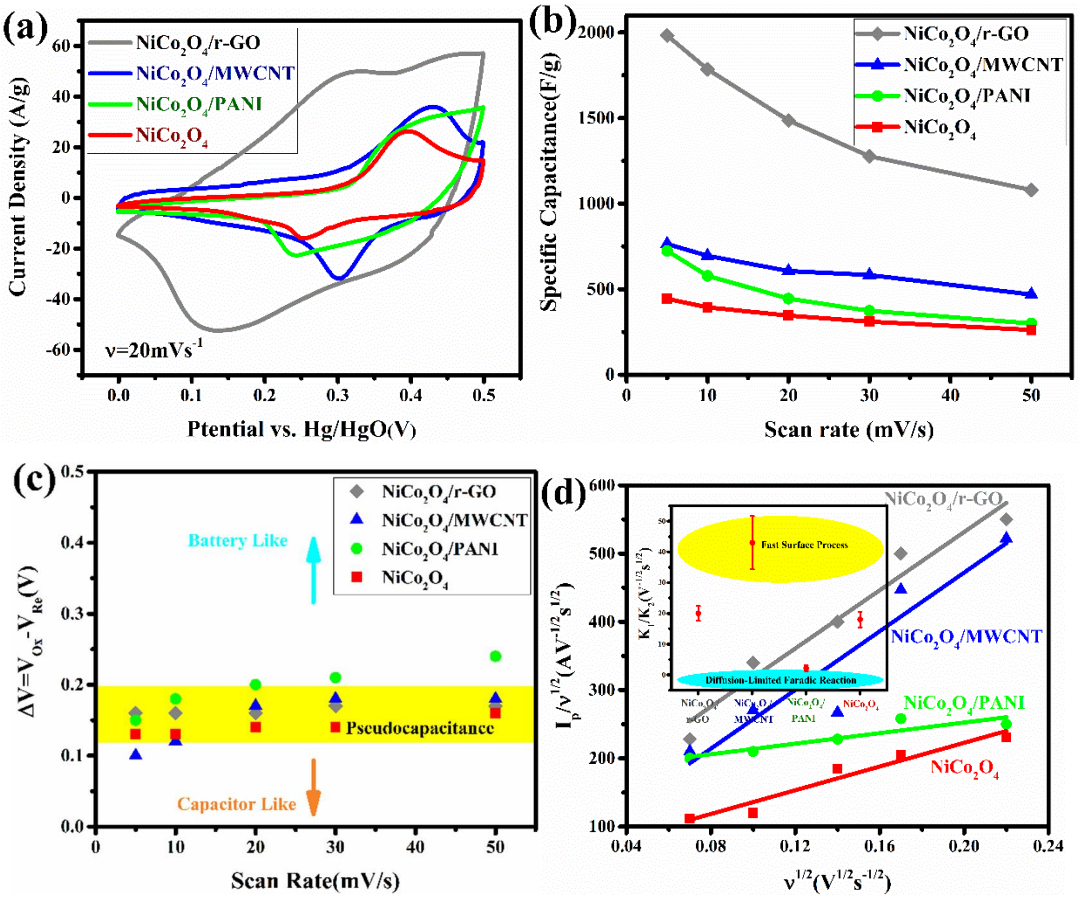

Figure 3: Evaluation of the electrochemical performance of the hybrid nanocomposites in a three-electrode configuration: (a) CV of $NiCo_2O_4$ cores, $NiCo_2O_4$/PANI, $NiCo_2O_4$/MWCNT and $NiCo_2O_4$/r-GO nanocomposites at scan rates of 20 mVs^{-1} in an aqueous 3 M KOH electrolyte solution. (b)Specific capacitances of $NiCo_2O_4$ nanocores, $NiCo_2O_4$/PANI, $NiCo_2O_4$/MWCNT and $NiCo_2O_4$/r-GO nanocomposites derived from CV measurements, (c) potential difference of faradic oxidation and reduction peaks versus various scan rates. (d) Polt of $I_p/v^{1/2}$ versus $v^{1/2}$; the isent polt of K_1/K_2

From the shapes of CV plots (see Figure S2) it can be inferred that the behavior of the developed nanocomposite materials is pseudocapacitive as confirmed by the presence of different redox peaks of both $NiCo_2O_4$ nanocores and nanocomposite electrodes from redox reactions in the alkaline medium, which would correspond to the reversible reactions of Ni^{2+}/Ni^{3+} and Co^{3+}/Co^{4+} transitions associated with $0H^-$ anions. As reported previously [16,17,25,35], the spinel structure of $NiCo_2O_4$ nanocores shows a potential window of 0 to 0.5 V in alkaline conditions, and their pseudo-capacitive behavior can be described by the following equations:

$$NiCo_2O_4 + H_2O + e^- \leftrightarrow 2CoOOH + NiOH \quad (1)$$

$$CoOOH + OH^- \leftrightarrow CoO_2 + H2O + e^- \quad (2)$$

$$NiOH + OH^- \leftrightarrow Ni(OH)_2 + e^- \quad (3)$$

The oxidation peak potentials of Ni^{2+}/Ni^{3+} and Co^{3+}/Co^{4+} transitions are so close one each other that is difficult to split them apart [17,64,65]. Even at high scan rates, CV plots show well-defined redox peaks, which points to the capability of the porous $NiCo_2O_4$ nanocores to sustain these fast redox reactions. It is also observed that the current density increases as the scan rate does and, consequently, the peak potential is progressively shifted in agreement with the low polarization and high power of the selected electrode nanomaterials [63]. As illustrated in Figure S2a, the cathodic peak is slightly shifted from 0.26 to 0.24 V as the scan rate increases from 5 to 50 mV s^{-1}, that is, the $NiCo_2O_4$ electrode can sustain very fast redox reactions. In addition, it is worth mentioning that the

Preprints (www.preprints.org) | NOT PEER-REVIEWED | Posted: 7 May 2019 doi:10.20944/preprints201905.0068.v1

constructed nanocomposite-based electrodes have low resistivity and good electrochemical reversibility.

In particular, for $NiCo_2O_4$/PANI nanocomposites, cathodic and anodic peaks progressively shift from 0.25 to 0.22 V and from 0.4 to 0.45 V at increasing scan rates, respectively, and the capacitance decreases thanks to the synergistic effect of the embedded pseudo-reactions and additional conductive pathways provided by PANI (Figure S2b). Similarity, anodic and cathodic peaks of $NiCo_2O_4$/MWCNT nanocomposites shift from 0.41 to 0.47 V and 0.31 to 0.28 V, respectively (Figure S2c). It has been demonstrated that porous MWCNTs networks and the subsequent stability of their electrical response greatly promote the due to from $NiCo_2O_4$ nanocores (Figure S2d).

The capacitances of porous $NiCo_2O_4$ nanocores, $NiCo_2O_4$/MWCNT, $NiCo_2O_4$/PANI and $NiCo_2O_4$/r-GO nanocomposites can be calculated from CV plots at different scan rates by the following relationship [64]:

$$C = \frac{\int IdV}{\mathrm{m}v\Delta V} \quad (4)$$

where C is the specific capacitance (F/g), ΔV is the potential window of CV (V), I is the current intensity (A), ν is the scan rate (V/s) m is the mass of loaded material (g) [65] (see Supplementary Materials for further details). The calculated specific capacitance of porous $NiCo_2O_4$ nanocores, $NiCo_2O_4$/MWCNT, $NiCo_2O_4$/PANI and $NiCo_2O_4$/r-GO-based nanoelectrodes are given in Figure 3b. As mentioned above, capacitances decrease as the scan rates increase, which can be attributed to the lower diffusion of electrolyte ions. At higher scan rates only the outer surfaces can contribute to the charge-discharge processes, which result in a lower effectiveness of the electro-active materials. As shown in Figure 3c, the potential difference of oxidation and reduction peaks ($\Delta V = V_{Ox} - V_{Re}$) [66] confirmed the pseudocapacitive behavior of the obtained hybrid nanoelectrodes This was additionally corroborated by analyzing the dependence of the electrical current with the scan rate as:

$$I_p = K_1\nu + K_2\nu^{1/2} \quad (5)$$

where $\nu[Vs^{-1}]$ is the scan rate. K_1 and K_2 coefficients are related to fast surface processes and diffusion limited faradic reactions, respectively. By plotting $I_p/\nu^{1/2}$ versus $\nu^{1/2}$, K_1 and K_2 can be obtained and the kinetics of the reaction determined (Figure 3d) [67].

In addition to specific capacitances (C_{sp}) calculated from CV curves, these can be alternatively obtained from galvanostatic charge/discharge (C/D) measurements, allowing a comparison and evaluation of the quality of the measurements. Figure 4a shows C/D plots of the different constructed nanoelectrodes at a current density within the potential range 0-0.5 V at 1 A/g (see Figure S3 for additional C/D plots at other current densities). The shape of C/D plots is non-linear as a consequence of the Co^{3+}/Co^{4+}, Ni^{2+}/Ni^{3+} ions redox reactions with OH^-.

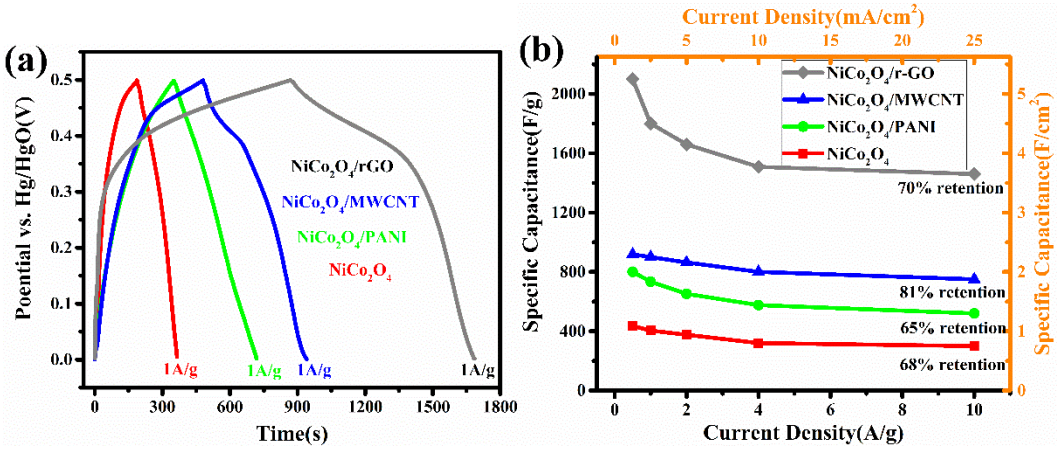

Figure 4: (a) Galvanostatic charge/discharge plots at current density 1A/g and (b) rate capability of, $NiCo_2O_4$ nanocores, $NiCo_2O_4$/PANI, $NiCo_2O_4$/MWCNTs, and $NiCo_2O_4$/r-GO nanostructured-based electrodes

C_{sp} can be calculated by means of the following equation:

Preprints (www.preprints.org) | NOT PEER-REVIEWED | Posted: 7 May 2019 doi:10.20944/preprints201905.0068.v1

$$C_{sp} = (I \times \Delta t)/(m \times \Delta V) \quad (6)$$

where I is the discharge current (A), Δt the discharge time (s), m the mass of loaded material (g), and ΔV the window potential (V). The obtained values for the different electrodes are in fair agreement with those previously obtained from CV data. From these data, a superior performance of the $NiCo_2O_4$/MWCNTs nanocomposite-based electrode compared to the $NiCo_2O_4$/PANI one is again noted, which is related to the advantageous structural features of MWCNTs; that is, the carbon-based material provides a faster electron transfer and a larger contact area for electrolyte ions and their subsequent penetration inside the hybrid storage system. Nevertheless, $NiCo_2O_4$ cores supported on ultrathin r-GO nanosheets electrode exhibit the largest specific capacitances. This outstanding performance might be attributed to the advantageous nanostructuration of this electrode. Specifically, the ultrathin carbon nanosheets of r-GO could provide numerous electro-active sites for redox reactions thanks to its extensive surface area. Besides, the open space inside $NiCo_2O_4$ cores provided by their mesoporous structure can serve as a reservoir for ions, whereas the presence of r-GO covering the $NiCo_2O_4$ cores would enhance the diffusion kinetics within the electrode; in other words, r-GO nanosheets may ensure an efficient contact between the surface of electroactive r-GO nanosheets and the electrolyte, which should allow a faster ion diffusion to the active sites for the redox reactions to proceed. Furthermore, the avoidance of binder and other conductive materials such as PVDF and carbon black powders in the compositions of this nanoelectrode, commonly added to prepare nickel foam-based commercial electrodes, can additionally improve the direct contact between r-GO sheets and $NiCo_2O_4$ cores, consequently, enhancing the intrinsic electrical conductivity.

A comparison of the electrochemical outputs of the present $NiCo_2O_4$/MWCNT and $NiCo_2O_4$-rGO nanocomposite-based electrodes with others previously obtained by different methodologies is shown in Table S1. In this regard, the method followed to obtain the $NiCo_2O_4$/MWCNT composites is faster, cost-effective and more reproducible than previous ones, and also leads to large capacitance of ca. 900 F/g at 1 A/g. For example, Liu *et al.* developed $NiCo_2O_4$/CNTs composites by a electrodeposition process and subsequent annealing treatment obtaining a capacitance of ca. 694F/g at 1 A/g and cycling stabilities of 79.6% [29]. Another multistep procedure including chemical co-deposition, calcination and thermal treatment was performed by Cai et al., in which a high concentration electrolyte 6M KOH was used to obtain a capacitance of 1038F/g at 0.5 A/g, with cycling stability of 100% [30]. On the other hand, Wang *et al.* developed $NiCo_2O_4$/r-GO composites by a self-assembled approach with capacitances of up to 835 F/g at 1 A/g and an outstanding cycling stability of ca. 100% but using much higher electrolyte concentrations (6 M KOH) [68]. Ma *et al*. reported a $NiCo_2O_4$/RGO (NCG) composite using a reflux method which delier a capacitance of 1186 F/g at 0.5 A/g, with a cycling stability of 97% [69]. In our case, using similar raw starting materials the simple and scalable manufacturing process here used allowed to obtain much larger capacitances of ca. 1760 F/g at 1 A/g with improved stability thanks to efficient contact between the electroactive material surfaces including r-GO nanosheets and the metal oxide NPs.

Additionally, cyclic tests were performed at 2 A/g to evaluate the cycling stability of the electroactive nanomaterials constituting the electrodes for long operation periods. For $NiCo_2O_4$ nanocores, a capacitance retention ability of 79% after 1000 cycles (Figure 5a) was measured, that is, the specific capacitance decrease from 376 to 317 F/g as a consequence of the deintercalation of the electrochemical species. Conversely, the cycling stability of $NiCo_2O_4$/PANI nanocomposites was larger, with slow decreases in capacitance after the first 500 cycles of operation from 648 to 504 F/g, with a total the capacitance retention of 77%. The cycling performance of the $NiCo_2O_4$/MWCNT-based nanoelectrode impressively showed a very stable performance with a specific capacitance of 860 F/g retained over 1000 cycles, corresponding to a loss of only 8% (Figure 5(a). This enhanced cycling stability is probably attributed to the uniform distribution of $NiCo_2O_4$ nanocores and MWCNTs along the electrode. Finally, the stability curve for the $NiCo_2O_4$/r-GO-based electrode showed that the specific capacitance decreased from 1560 to 1420 F/g (9% loss) due to the activation process resulting from the complete intercalation between $NiCo_2O_4$ nanocores and r-GO nanosheets with electrolyte ions.

Preprints (www.preprints.org) | NOT PEER-REVIEWED | Posted: 7 May 2019 doi:10.20944/preprints201905.0068.v1

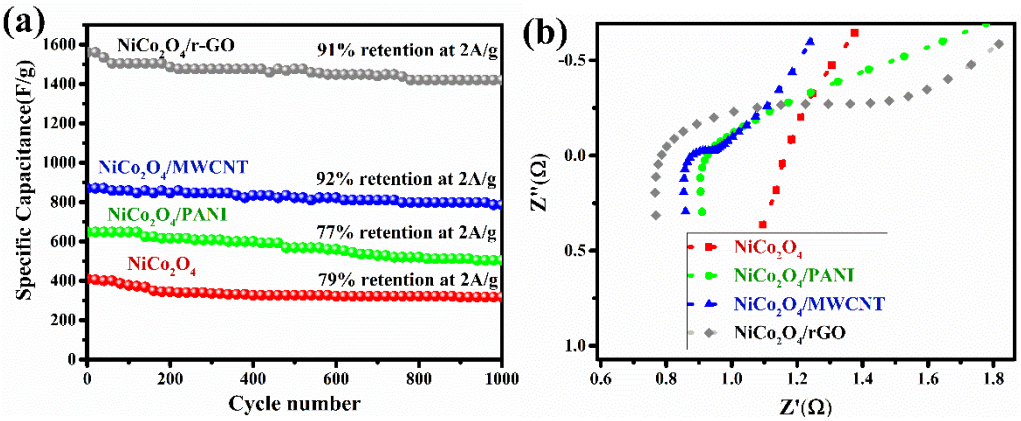

Figure 5: (a) Long-term cycling stability over 1000 C/D cycles and (b) Nyquist plot of $NiCo_2O_4$ nanocores, $NiCo_2O_4$/PANI, $NiCo_2O_4$/MWCNTs, and, $NiCo_2O_4$/r-GO nanocomposite-based electrodes.

Electrochemical impedance spectroscopy measurements recorded in the frequency range from 100 kHz to 0.01 Hz were also done (Figure S4). Based on EIS data, capacitors do not display an ideal behavior, indeed, they act as a constant phase element (CPE) [70], which is a typical behavior shown by double layer capacitors in real cells [71], In the present case, this is provided by the carbon-based nanomaterials present in the nanocomposite structures. CPE were applied in the equivalent circuit for the simulation of the experimental impedance data [72-74]. The impedance of a CPE is given by:

$$\frac{1}{Z} = Q^0(j\omega)^n \quad (7)$$

where Q^0 is the absolute value of the admittance ($1/|Z|$) at ω = 1 rad/s [75]. When the exponent is n = 1, the latter equation describes the impedance of a capacitor, so the constant $Q^0 = C$ is the capacitance. In this manner, the present impedance spectra can be interpreted and modeled using equivalent circuits according to the structure of the nanocomposites and the different layers of the materials present within their structure. This modelization was carried out by means of Zview software. To do that, EIS data were fitted in a first step to a simple equivalent circuit model and, then, additional components were added until reaching the best outcome. These equivalent circuits are illustrated in Figure S4 (left column), the so-called Nyquist impedance plots, in which R_1, L_1 and L_2 are the solution resistance, the internal charge of electrode, and the charge transfer resistance, respectively. The value of R_1 is attributed to the ionic and electronic resistance, the intrinsic resistance, and the diffusion and contact resistance of the electrode/current collector interface. Nyquist plots provide information about the resistance of electrolyte, pre-stored charge in the electrode, the capacitance and resistance of each nanomaterial within the nanoelectrode, and the capacitance of the resulting supercapacitor. Thus, the resulting electrical circuit was used to evaluate the equivalent capacitor. In this manner, it is possible to evaluate the capacitances of the resulting equivalent circuits (see Supplementary Materials for additional information) in order to compare the different nanocomposite electrodes. The fitting data based on the relevant equivalent circuits as equivalent capacitors are given in Table S2.

The phase (φ) was calculated as:

$$\tan(\varphi) = Z''/Z' \quad (8)$$

Bode plots (Figure S4c,f,i,l) show that the capacitance decreases as the frequency increases for all nanocomposite-based electrodes; each change in the slope corresponds to a layer of material within the supercapacitor structure. At high-frequencies all supercapacitors possess a pure resistance-like behavior indicating that electrolyte ions probably cannot penetrate into mesopores at high frequencies [7]. In addition, each maximum in the phase plots (Figure S4b,e,h,k) also represents a layer in the supercapacitor. Therefore, both Bode and phase plots confirm that the supercapacitors are also composed of an electric double layer provided by the presence of the carbon-based nanomaterials.

Figure S4a-c shows the existence of one slope and a smooth peak in Bode and phase plots, respectively, for the bare $NiCo_2O_4$-based electrode, that is, the nanoelectrode is only formed by one material layer. In Figure S4d, the Nyquist plot for $NiCo_2O_4$/PANI-based electrode represents two impedances connected in parallel, and the corresponding Bode and phase plots confirmed the presence of two layers of material for this supercapacitor (Figure S4e,f). For the $NiCo_2O_4$/MWCNT based-electrode, the Nyquist plot is indicative of two impedances connected in series, each one with a resistive and capacitive effect (Figure S4g). It is also observed from Bode and phase plots that MWCNTs provide a high-power electrode thanks to its good electrical conductivity and readily accessible surface area (Figure S4h,i). Finally, as shown in Figure S4j,l, Nyquist, Bode and phase plots, and the equivalent circuit for the $NiCo_2O_4$/r-GO nanocomposite-based electrode confirm the existence of a double layer structure. The charge-transfer resistance was assigned nearest the solution interface and the other resistance to the binder. Another possible reason for the observed enhancement of efficiency in this nanostructure can be originated from the interfacial properties between r-GO nanosheets and $NiCo_2O_4$ nanocores; in particular, the r-GO skeleton retains a high electrical conductivity even for very thick electrodes and prevents cycling-induced degradation [76].

4. Conclusion

Porous spinel $NiCo_2O_4$ nanocores were prepared by a simple and controlled solvothermal method. The advantages of using $NiCo_2O_4$ nanocores as the main electroactive material reside in their good electrical conductivity, rich electroactive behavior, stable spinel structure, and environmentally benign use. The introduction of carbon-based nanomaterials of different nature in the nanostructure of the developed electrodes allows incorporate the benefits of electrical double layer conductive materials to complement the action and performance of the redox reactions supported by the porous metal oxide core nanomaterial. In this manner, the incorporation of an organic conductive polymer such as PANI via in situ polymerization to obtain a $NiCo_2O_4$/PANI nanocomposite resulted in an important enhancement of the capacitance up to 734 F/g at 1 A/g, in comparison with the bare $NiCo_2O_4$ nanocore-based single electrode. When incorporating MWCNTs, the formed MWCNT network within the nanocomposite improves its electrical conductivity and consequently, the ion transfer speed, thus, giving rise to a $NiCo_2O_4$/MWCNTs supercapacitor with additional enhancements in specific capacitance (up to ca. 900 F/g at 1 A/g) and stable life cycles (91 % of capacitance retention) for long operation periods. Also, it was shown that the morphology of the electrode material has a substantial influence on the ion transfer speed and the capacity of charge storage. This was demonstrated when performed the electrochemical deposition of r-GO onto a modified nickel foam covered with $NiCo_2O_4$ nanocores to obtain a $NiCo_2O_4$/r-GO composite, which holds a maximum specific capacitance of 1760 F/g at 1 A/g. In this preparation two common materials such as carbon black and PVDF regularly used in the preparation of commercial supercapacitor electrodes were not required, which involves the reduction of the associated costs of production while avoids at the same time inefficient contacts between the electroactive and conducting materials. Therefore, the obtained superior properties of the present active nanoelectrodes make them an interesting alternative to those currently used, and the flexibility of the production methodologies should allow the fabrication of additional electro-active materials with even improved properties.

Supplementary data: Supplementary data to this article can be found online at https://doi.org/10.1016/j.elecacta.2019.

Acknowledgements: This work was supported by Agencia Estatal de Investigación (AEI) through Project MAT2016-80266-R, and Xunta de Galicia (Grupo de Referencia Competitiva ED431C 2018/26; Agrupación Estratégica en Materiales-AEMAT ED431E 2018/08). FEDER funds are also acknowledged.

Conflicts of Interest: The authors declare no conflict of interest.

References

1. Zhou, C.; Zhang, Y.; Li, Y.; Liu, J. Construction of High-Capacitance 3D CoO@Polypyrrole Nanowire Array Electrode for Aqueous Asymmetric Supercapacitor Cheng. Nano Lett. 2013, 13, 2078–2085.

2. Wang, C.; Zhou, E.; He, W.; Deng, X.; Huang, J.; Ding, M.; Wei, X.; Liu, X.; Xu, X. NiCo2O4-Based Supercapacitor Nanomaterials. Nanomaterials 2017, 7, 41.
3. Shi, Xiaoze.; Zhang, Shuai.; Chen, Xuecheng.; Mijowska, Ewa. Evaluation of Nanoporous Carbon Synthesized from Direct Carbonization of a Metal–Organic Complex as a Highly Effective Dye Adsorbent and Supercapacitor: Nanomaterials 2019, 9, 601; doi:10.3390/nano9040601
4. Rani, Janardhanan. R..; Thangavel, Ranjith; Oh, Se-I; Lee, Yun Sung; Jang, Jae-Hyung. An Ultra-High-Energy Density Supercapacitor;Fabrication Based on Thiol-unctionalized Graphene Oxide Scrolls. Nanomaterials 2019, 9, 148; doi:10.3390/nano9020148.
5. Zhang, L. L.; Zhao, X. S. Carbon-Based Materials as Supercapacitor Electrodes. *Chem. Soc. Rev.* **2009**, *38*, 2520–2531.
6. Yang, Hanbin; Zhu, Xinqiang; Zhu, Enhui; Lou, Gaobo; Wu, Yatao; Lu, Yingzhuo; Wang, Hanyu; Electrochemically Stable Cobalt–Zinc Mixed Oxide/Hydroxide Hierarchical Porous Film electrode for High-Performance Asymmetric Supercapacitor. Nanomaterials 2019, 9, 345; doi:10.3390/nano9030345.
7. Wang, G.; Zhang, L.; Zhang, J. A Review of Electrode Materials for Electrochemical Supercapacitors. Chem. Soc. Rev. 2012, 41, 797–828.
8. Chen, K.; Yin, S.; Xue, D. A Binary AxB1-x Ionic Alkaline Pseudocapacitor System Involving Manganese, Iron, Cobalt, and Nickel: Formation of Electroactive Colloids via in Situ Electric Field Assisted Coprecipitation. Nanoscale 2015, 7, 1161–1166.
9. Ma, Y.; Hou, C.; Zhang, H.; Qiao, M.; Chen, Y.; Zhang, H.; Zhang, Q.; Guo, Z. Morphology-Dependent Electrochemical Supercapacitors in Multi- Dimensional Polyaniline Nanostructures. Mater. Chem. A 2017, 5, 14041–14052.
10. Ma, L.; Su, L.; Zhang, J.; Zhao, D.; Qin, C.; Jin, Z.; Zhao, K. A Controllable Morphology GO/PANI/Metal Hydroxide Composite for Supercapacitor. J. Electroanal. Chem. 2016, 777, 75–84.
11. Shown, I.; Ganguly, A.; Chen, L. C.; Chen, K. H. Conducting Polymer-Based Flexible Supercapacitor. Energy Sci. Eng. 2015, 3, 1–25.
12. Tan, Y.; Zhang, Y.; Kong, L.; Kang, L.; Ran, F. Nano-Au@PANI Core-Shell Nanoparticles via in-Situ Polymerization as Electrode for Supercapacitor. J. Alloys Compd. 2017, 722, 1–7.
13. Prateek; Thakur, V. K.; Gupta, R. K. Recent Progress on Ferroelectric Polymer-Based Nanocomposites for High Energy Density Capacitors: Synthesis, Dielectric Properties, and Future Aspects. Chem. Rev. 2016, 116, 4260–4317.
14. Qorbani, M.; Naseri, N.; Moshfegh, A. Z. Hierarchical Co3O4/Co(OH)2/ Nanoflakes as a Supercapacitor Electrode: Experimental and Semi-Empirical Model. ACS Appl. Mater. Interfaces 2015, 7 (21), 11172–11179.
15. Settanni, G.; Zhou, J.; Suo, T.; Schöttler, S.; Landfester, K.; Schmid, F.; Mailänder, V. Porous Nanoarchitectures of Spinel-Type Transition Metal Oxides for Electrochemical Energy Storage Systems. Phys. Chem. Chem. Phys. 2015, 1–14.
16. Yuan, C.; Li, J.; Hou, L.; Zhang, X.; Shen, L.; Lou, X. W. Ultrathin Mesoporous NiCo 2O 4 Nanosheets Supported on Ni Foam as Advanced Electrodes for Supercapacitors. Adv. Funct. Mater. 2012, 22, 4592–4597.
17. Zhu, Y.; Ji, X.; Wu, Z.; Song, W.; Hou, H.; Wu, Z.; He, X.; Chen, Q.; Banks, C. E. Spinel NiCo2O4for Use as a High-Performance Supercapacitor Electrode Material: Understanding of Its Electrochemical Properties. J. Power Sources 2014, 267, 888–900.
18. Salunkhe, R. R.; Kaneti, Y. V; Yamauchi, Y. Metal − Organic Framework-Derived Nanoporous Metal Oxides toward Supercapacitor Applications: Progress and Prospects. ACS Nano 2017, 11, 5293–5308.
19. He, C.; Wu, S.; Zhao, N.; Shi, C.; Liu, E.; Li, J. Carbon-Encapsulated Fe3O4 Nanoparticles as a High-Rate Lithium Ion Battery Anode Material. ACS Nano 2013, 7, 4459–4469.
20. Salunkhe, R. R.; Tang, J.; Kobayashi, N.; Kim, J.; Ide, Y.; Tominaka, S.; Kim, J. H.; Yamauchi, Y. Ultrahigh Performance Supercapacitors Utilizing Core-Shell Nanoarchitectures from a Metal-Organic Framework-Derived Nanoporous Carbon and a Conducting Polymer. Chem. Sci. 2016, 7, 5704–5713.
21. Bo, A.; Tao, Z.; Li, W.; Kai, J.; Matthew, Z. NiO Mesoporous Nanowalls Grown on RGO Coated Nickel Foam as High Performance Electrodes for Supercapacitors and Biosensors. Electrochim. Acta 2016.
22. Tang, K.; Fu, L.; White, R. J.; Yu, L.; Titirici, M. M.; Antonietti, M.; Maier, J. Hollow Carbon Nanospheres with Superior Rate Capability for Sodium-Based Batteries. Adv. Energy Mater. 2012, 2, 873–877.
23. Wu, S.; Xu, R.; Lu, M.; Ge, R.; Iocozzia, J.; Han, C.; Jiang, B.; Lin, Z. Graphene-Containing Nanomaterials for Lithium-Ion Batteries. Adv. Energy Mater. 2015, 5, 1–40.

24. Jiang, B.; Han, C.; Li, B.; He, Y.; Lin, Z. In-Situ Crafting of ZnFe2O4Nanoparticles Impregnated within Continuous Carbon Network as Advanced Anode Materials. ACS Nano 2016, 10, 2728–2735.
25. Wu, Z.; Zhu, Y.; Ji, X. NiCo2O4-Based Materials for Electrochemical Supercapacitor. Mater. Chem. A 2016, No. 1, 3504–3512.
26. Ma, W.; Chen, S.; Yang, S.; Chen, W.; Weng, W.; Cheng, Y.; Zhu, M. Flexible All-Solid-State Asymmetric Supercapacitor Based on Transition Metal Oxide Nanorods/Reduced Graphene Oxide Hybrid Fibers with High Energy Density. Carbon N. Y. 2017, 113, 151–158.
27. Hu, Y. S.; Kienle, L.; Guo, Y. G.; Maier, J. High Lithium Electroactivity of Nanometer-Sized Rutile TiO2. Adv. Mater. 2006, 18, 1421–1426.
28. ARICÒ, A. S.; BRUCE, P.; SCROSATI, B.; TARASCON, J.-M.; SCHALKWIJK5, W. VAN. Nanostructured Materials for Advanced Energy Conversion and Storage Devices. Nat. Mater. 2005, 4, 366–377.
29. Liu, W. W.; Lu, C.; Liang, K.; Tay, B. K. A Three Dimensional Vertically Aligned Multiwall Carbon Nanotube/NiCo2O4core/Shell Structure for Novel High-Performance Supercapacitors. J. Mater. Chem. A 2014, 2, 5100–5107.
30. Cai, F.; Kang, Y.; Chen, H.; Li, Q. Hierarchical CNT@NiCo2O4 Core–shell Hybrid Nanostructure for High-Performance Supercapacitors. J. Mater. Chem. A 2014, 2, 11509–11515.
31. Mitchell, E.; Jimenez, A.; Gupta, R. K.; Gupta, B. K.; Ramasamy, K.; Shahabuddin, M.; Mishra, S. R. Ultrathin Porous Hierarchically Textured NiCo2O4-Graphene Oxide Flexible Nanosheets for High-Performance Supercapacitors. New J. Chem. 2015, 39, 2181–2187.
32. Jiang, H.; Yang, K.; Ye, P.; Huang, Q.; Wang, L.; Li, S. Optimized NiCo2O4/RGO Hybrid Nanostructures on Carbon Fiber as an Electrode for Asymmetric Supercapacitors. RSC Adv. 2018, 8, 37550–37556.
33. Carriazo, D.; Patiño, J.; Gutiérrez, M. C.; Ferrer, M. L.; Del Monte, F. Microwave-Assisted Synthesis of NiCo2O4-Graphene Oxide Nanocomposites Suitable as Electrodes for Supercapacitors. RSC Adv. 2013, 3, 13690–13695.
34. Li, D.; Gong, Y.; Wang, M.; Pan, C. Preparation of Sandwich-like NiCo2O4/RGO/NiO Heterostructure on Nickel Foam for High-Performance Supercapacitor Electrodes. Nano-Micro Lett. 2017, 9, 1–9.
35. Shen, L.; Yu, L.; Yu, X. Y.; Zhang, X.; Lou, X. W. D. Self-Templated Formation of Uniform NiCo2O4hollow Spheres with Complex Interior Structures for Lithium-Ion Batteries and Supercapacitors. Angew. Chemie - Int. Ed. 2015, 54, 1868–1872.
36. Avilés, F.; Cauich-Rodríguez, J. V.; Moo-Tah, L.; May-Pat, A.; Vargas-Coronado, R. Evaluation of Mild Acid Oxidation Treatments for MWCNT Functionalization. Carbon N. Y. 2009, 47, 2970–2975.
37. ISMAIL, A. F.; GOH, P. S.; TEE, J. C.; SANIP, S. M.; AZIZ, M. A Review of Purification Techniques for Carbon Nanotubes. Nano 2008, 03, 127–143.
38. Silambarasan, D.; Surya, V. J.; Vasu, V.; Iyakutti, K. Single Walled Carbon Nanotube − Metal Oxide Nanocomposites for Reversible and Reproducible Storage of Hydrogen. ACS Appl. Mater. Interfaces 2013, 3, 11419–11426.
39. Datsyuk, V.; Kalyva, M.; Papagelis, K.; Parthenios, J.; Tasis, D.; Siokou, A.; Kallitsis, I.; Galiotis, C. Chemical Oxidation of Multiwalled Carbon Nanotubes. Carbon N. Y. 2008, 46, 833–840.
40. Zhu, C.; Chou, S.; He, S.; Liao, W.; Chen, C. Synthesis of Core/Shell Metal Oxide/Polyaniline Nanocomposites and Hollow Polyaniline Capsules. Nanotechnology 2007, 18, 275604.
41. Marcano, D.; Kosynkin, D.; Berlin, J. Improved Synthesis of Graphene Oxide. ACS Nano 2010, 4, 4806–4814.
42. Moozarm, P.; Pei, W.; Lorestani, F.; Mahmoudian, M. R.; Alias, Y. Sensors and Actuators B : Chemical Electrodeposition of Copper Oxide / Polypyrrole / Reduced Graphene Oxide as a Nonenzymatic Glucose Biosensor. sensors Actuators Chem. 2015, 209, 100–108.
43. Chen, K.; Chen, L.; Chen, Y.; Bai, H.; Li, L. Three-Dimensional Porous Graphene-Based Composite Materials: Electrochemical Synthesis and Application. J. Mater. Chem. 2012, 22, 20968.
44. Das, A. K.; Layek, R. K.; Kim, N. H.; Jung, D.; Lee, J. H. Reduced Graphene Oxide (RGO)-Supported NiCo 2 O 4 Nanoparticles: An Electrocatalyst for Methanol Oxidation. Nanoscale 2014, 6, 10657.
45. Pandi, K.; Sivakumar, M.; Chen, S.; Cheng, Y.; Chen, T. Hydrothermal Synthesis of Carbon Coated NiCo 2 O 4 Nano Flower for the Electrochemical Oxidation of Sulfite in Real Sample. Int. J. Electrochem. Sci. 2018, 13, 1227–1240.
46. Li, D.; Gong, Y.; Zhang, Y.; Luo, C.; Li, W.; Fu, Q.; Pan, C. Facile Synthesis of Carbon Nanosphere/NiCo2O4 Core-Shell Sub-Microspheres for High Performance Supercapacitor. Sci. Rep. 2015, 5 (August).

47. Ko, T. H.; Radhakrishnan, S.; Choi, W. K.; Seo, M. K.; Kim, B. S. Core/Shell-like NiCo2O4-Decorated MWCNT Hybrids Prepared by a Dry Synthesis Technique and Its Supercapacitor Applications. Mater. Lett. 2016, 166, 105–109.
48. Miao, Y.; Fan, W.; Chen, D.; Liu, T. High-Performance Supercapacitors Based on Hollow Polyaniline Nano Fi Bers by Electrospinning. ACS Appl. Mater. Interfaces 2013, 5, 4423–4428.
49. Huang, M.; Li, F.; Ji, J. Y.; Zhang, Y. X.; Zhao, X. L.; Gao, X. Facile Synthesis of Single-Crystalline NiO Nanosheet Arrays on Ni Foam for High-Performance Supercapacitors. CrystEngComm 2014, 16, 2878–2884.
50. Stobinski, L.; Lesiak, B.; Malolepszy, A.; Mazurkiewicz, M.; Mierzwa, B.; Zemek, J.; Jiricek, P.; Bieloshapka, I. Graphene Oxide and Reduced Graphene Oxide Studied by the XRD, TEM and Electron Spectroscopy Methods. J. Electron Spectros. Relat. Phenomena 2014, 195, 145–154.
51. Jabeen, N.; Xia, Q.; Yang, M.; Xia, H. Unique Core − Shell Nanorod Arrays with Polyaniline Deposited into Mesoporous NiCo 2 O 4 Support for High-Performance Supercapacitor Electrodes. ACS Appl. Mater. Interfaces 2016, 8, 6093–6100.
52. Umeshbabu, E.; Rajeshkhanna, G.; Justin, P.; Rao, G. R. Magnetic, Optical and Electrocatalytic Properties of Urchin and Sheaf-like NiCo2O4nanostructures. Mater. Chem. Phys. 2015, 165, 235–244.
53. Mensing, J. P.; Lomas, T.; Tuantranont, A. Ammonia Strengthened Graphene/CNT-Wrapped Polyaniline-Nanofiber Composites Loaded with Palladium Nanoparticles for Coin Cell Supercapacitors. Electrochim. Acta 2018, 263, 17–25.
54. Cabezas, A. L.; Zhang, Z. Bin; Zheng, L. R.; Zhang, S. L. Morphological Development of Nanofibrillar Composites of Polyaniline and Carbon Nanotubes. Synth. Met. 2010, 160, 664–668.
55. Wang, Q.; Yao, Q.; Chang, J.; Chen, L. Enhanced Thermoelectric Properties of CNT/PANI Composite Nanofibers by Highly Orienting the Arrangement of Polymer Chains. J. Mater. Chem. 2012, 22, 17612.
56. Liu, Z. Q.; Xiao, K.; Xu, Q. Z.; Li, N.; Su, Y. Z.; Wang, H. J.; Chen, S. Fabrication of Hierarchical Flower-like Super-Structures Consisting of Porous NiCo2O4 Nanosheets and Their Electrochemical and Magnetic Properties. RSC Adv. 2013, 3, 4372–4380.
57. López-Lorente, A. I.; Simonet, B. M.; Valcárcel, M. Raman Spectroscopic Characterization of Single Walled Carbon Nanotubes: Influence of the Sample Aggregation State. Analyst 2014, 139, 290–298.
58. Bissett, M. A.; Barlow, A. J.; Shapter, J. G.; Quinton, J. S. Raman Characterisation of Carbon Nanotubes Grown by Plasma Enhanced Chemical Vapour Deposition. Adv. Mater. Nanotechnol. 2012, 700 (September 2014), 112–115.
59. Muhammad Hafiz, S.; Ritikos, R.; Whitcher, T. J.; Md. Razib, N.; Bien, D. C. S.; Chanlek, N.; Nakajima, H.; Saisopa, T.; Songsiriritthigul, P.; Huang, N. M.; et al. A Practical Carbon Dioxide Gas Sensor Using Room-Temperature Hydrogen Plasma Reduced Graphene Oxide. Sensors Actuators, B Chem. 2014, 193 (January), 692–700.
60. How, G. T. S.; Pandikumar, A.; Ming, H. N.; Ngee, L. H. Highly Exposed {001} Facets of Titanium Dioxide Modified with Reduced Graphene Oxide for Dopamine Sensing. Sci. Rep. 2014, 4 (June).
61. Thommes, M.; Kaneko, K.; Neimark, A. V.; Olivier, J. P.; Rodriguez-Reinoso, F.; Rouquerol, J.; Sing, K. S. W. Physisorption of Gases, with Special Reference to the Evaluation of Surface Area and Pore Size Distribution (IUPAC Technical Report). Pure Appl. Chem. 2015, 87, 1051–1069.
62. Vijayakumar, S.; Lee, S.; Ryu, K. Hierarchical CuCo 2 O 4 Nanobelts as a Supercapacitor Electrode with High Areal and Speci Fi c Capacitance. Electrochim. Acta 2015, 182, 979–986.
63. Khalid, S.; Cao, C.; Wang, L.; Zhu, Y. Microwave Assisted Synthesis of Porous NiCo2O4 Microspheres: Application as High Performance Asymmetric and Symmetric Supercapacitors with Large Areal Capacitance. Sci. Rep. 2016, 6 (October 2015), 1–13.
64. Singh, R. N.; Koenig, J.; Poillerat, G.; Chartier, P.; Soc, J. E.; Singh, R. N.; Koenig, J.; Poillerat, G.; Chartier, P. Electrochemical Studies on Protective Thin Co3 O4 and NiCo2O4 Films Prepared on Titanium by Spray Pyrolysis for Oxygen Evolution Electrochemical Studies on Protective Thin C0304 and NiC0204 Films Prepared on Titanium by Spray Pyrolysis for Oxygen Evolutio. J. elctrochemical Soc. 1990, 137, 1408–1413.
65. Meher, S. K.; Justin, P.; Rao, G. R. Microwave-Mediated Synthesis for Improved Morphology and Pseudocapacitance Performance of Nickel Oxide. ACS Appl. Mater. Interfaces 2011, 3, 2063–2073.
66. Dong, L.; Xu, C.; Yang, Q.; Fang, J.; Li, Y.; Kang, F. High-Performance Compressible Supercapacitors Based on Functionally Synergic Multiscale Carbon Composite Textiles. J. Mater. Chem. A 2015, 3, 4729–4737.

67. Al-Rubaye, S.; Rajagopalan, R.; Dou, S. X.; Cheng, Z. Facile Synthesis of a Reduced Graphene Oxide Wrapped Porous NiCo2O4composite with Superior Performance as an Electrode Material for Supercapacitors. J. Mater. Chem. A 2017, 5, 18989–18997.
68. Qorbani, M.; Chou, T.; Lee, Y. Layer Partially Reduced Graphene Oxide Hybrids : Towards Highly Stable Asymmetric Supercapacitors †. J. Mater. Chem. A Mater. energy Sustain. 2017, 00, 1–9.
69. Come, J.; Taberna, P.; Hamelet, S.; Masquelier, C.; Simon, P. Electrochemical Kinetic Study of LiFePO 4 Using Cavity Microelectrode. 2011, 158, 1090–1093.
70. Wang, H. W.; Hu, Z. A.; Chang, Y. Q.; Chen, Y. L.; Wu, H. Y.; Zhang, Z. Y.; Yang, Y. Y. Design and Synthesis of NiCo2O4-Reduced Graphene Oxide Composites for High Performance Supercapacitors. J. Mater. Chem. 2011, 21, 10504–10511.
71. Ma, L.; Shen, X.; Ji, Z.; Cai, X.; Zhu, G.; Chen, K. Porous NiCo2O4nanosheets/Reduced Graphene Oxide Composite: Facile Synthesis and Excellent Capacitive Performance for Supercapacitors. J. Colloid Interface Sci. 2015, 440, 211–218.
72. Oldham, K. B. The RC Time "Constant" at a Disk Electrode. Electrochem. commun. 2004, 6, 210–214.
73. Jorcin, J. B.; Orazem, M. E.; Pébère, N.; Tribollet, B. CPE Analysis by Local Electrochemical Impedance Spectroscopy. Electrochim. Acta 2006, 51, 1473–1479.
74. Kim, C. H.; Pyun, S. Il; Kim, J. H. An Investigation of the Capacitance Dispersion on the Fractal Carbon Electrode with Edge and Basal Orientations. Electrochim. Acta 2003, 48, 3455–3463.
75. Vogelsang, J.; Strunz, W. The Evaluation of Experimental Dielectric Data of Barrier Coatings by Means of Different Models. Electrochim. Acta 2001, 46, 3619–3625.
76. Guan, H.; Fan, L. Z.; Zhang, H.; Qu, X. Polyaniline Nanofibers Obtained by Interfacial Polymerization for High-Rate Supercapacitors. Electrochim. Acta 2010, 56, 964–968.
77. NIST. Guide for the Use of the International System of Units (SI). Med. Sci. Sport. Exerc. 1999, 31, 198–205.
78. Yoon, Y.; Lee, K.; Lee, H. Low-Dimensional Carbon and MXene-Based Electrochemical Capacitor Electrodes. Nanotechnology 2016, 27, 172001.